RESEARCH ARTICLE

small methods
www.small-methods.com

Multiple RNA Rapid In Situ Imaging Based on Cas9 Code Key System

Ruiwei Hu, Wei Yang, Jia Li, Lanxin Jiang, Menghan Li, Mengxuan Zhang, Yuexi Kang, Xiaoxue Cheng, Shasha Zhu, Lina Zhao, Wen He, Minghui Guo, Shijia Ding, Haiping Wu,* and Wei Cheng**

Existing RNA in situ imaging strategies mostly utilize parallel repetitive nucleic acid self-assembly to achieve multiple analysis, with limitations of complicated systems and cumbersome steps. Here, a Cas9 code key system with key probe (KP) encoder and CRISPR/Cas9 signal exporter is developed. This system triggers T-protospacer adjacent motif (T-PAM structural transitions of multiple KP encoders to form coding products with uniform single-guide RNA (sgRNA) target sequences as tandem nodes. Only single sgRNA/Cas9 complex is required to cleave multiple coding products, enabling efficient "many-to-one" tandem signaling, and non-collateral cleavage activity-dependent automatic signaling output through active introduction of mismatched bases. Compared with conventional parallel multiple signaling analysis model, the proposed system greatly simplifies reaction process and enhances detection efficiency. Further, a rapid multiple RNA in situ imaging system is developed by combining the Cas9 code key system with a T-strand displacement amplification (T-SDA) signal amplifier. The constructed system is applied to tumor cells and clinicopathology slices, generating clear multi-mRNA imaging profiles in less than an hour with just one step. Therefore, this work provides reliable technical support for clinical tumor typing and molecular mechanism investigation.

1. Introduction

Malignant tumor exhibits a universal and crucial phenotypic feature of high heterogeneity due to cumulative variation, genetic drift, and pressure selection during the continuous evolution.[1–5] The remarkable heterogeneity is manifested by significant differences in molecular expression between different foci and cell subpopulations within foci.[5–7] Obtaining heterogeneity molecular profile serves as an essential basis for precise molecular typing and clinical decision-making in tumor diagnosis and treatment.[3,8–10] RNA, as the core link of central law, contains abundant biological information between gene transcription and protein translation, and is increasingly regarded as an indispensable molecule for tumor typing.[11,12] Several studies have confirmed that the abnormal expression of RNA in tumor cell is intimately associated with tumorigenesis, drug sensitivity, and prognostic assessment.[13,14] Moreover, the homogeneity feature of tumors hints that single RNA expression level change fails to explore the whole landscape of tumor information. In contrast, the synergistic analysis of multiple RNA may offer greater accuracy in obtaining precise typing profile.[11,15–17] Therefore, multiple RNA in situ analysis would provide more comprehensive information support for clinical tumor typing, which is also an urgent demand for clinical molecular diagnosis.

Currently, in situ RNA analysis techniques include spatial transcriptome sequencing, in situ optical imaging, and others.[12,18] Among them, in situ sequencing technology relies on complex spatial barcode hybridization and sequencing read, with limited single-cell resolution, thus preventing widespread clinical application.[19,20] Existing RNA in situ imaging techniques, such as RNAscope,[21,22] Stellaris RNA FISH,[23] π-FISH rainbow,[24] etc., are increasingly receiving extensive attention from researchers due to the advantages of facile optical encoding and single-cell resolution. Those strategies mainly rely on RNA directly triggering the subsequent complicated self-assembly of nucleic acid framework, which is combined with reporter probe to

R. Hu, J. Li, L. Jiang, Y. Kang, X. Cheng, S. Zhu, W. Cheng
The Center for Clinical Molecular Medical Detection
The First Affiliated Hospital of Chongqing Medical University
Chongqing 400042, China
E-mail: chengwei@hospital.cqmu.edu.cn
R. Hu, M. Li, M. Zhang, L. Zhao, W. He, M. Guo, S. Ding, H. Wu, W. Cheng
Key Laboratory of Clinical Laboratory Diagnostics (Ministry of Education)
College of Laboratory Medicine
Chongqing Medical University
Chongqing 400016, China
E-mail: dingshijia@cqmu.edu.cn; cqmuwhp@stu.cqmu.edu.cn
W. Yang
Laboratory Medicine Center
Department of Clinical Laboratory
Zhejiang Provincial People's Hospital (Affiliated People's Hospital)
Hangzhou Medical College
Hangzhou 310014, China

The ORCID identification number(s) for the author(s) of this article can be found under https://doi.org/10.1002/smtd.202400195

DOI: 10.1002/smtd.202400195

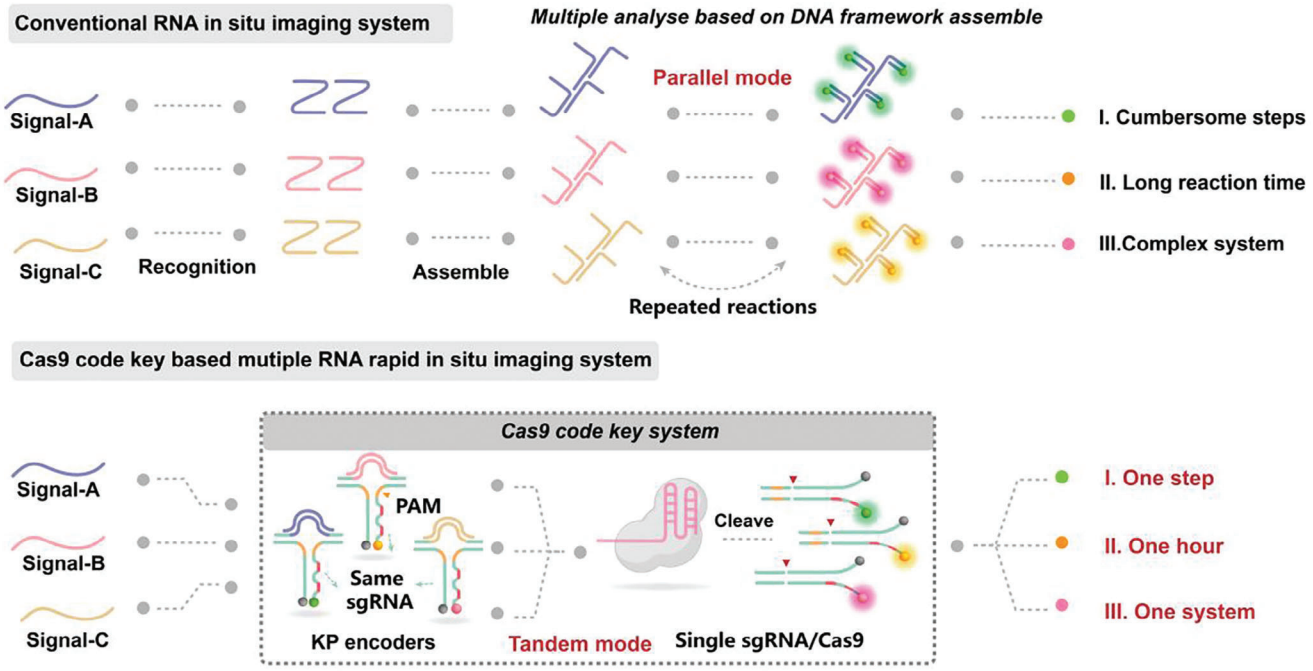

Scheme 1. Schematic diagrams of signaling pathways for the conventional RNA in situ imaging system and the Cas9 code key-based multiple RNA rapid in situ imaging system.

generate a highly sensitive in situ detection signal. Although multiple RNA analyses could be achieved through parallel repeated reactions, the above strategies greatly complicate reaction system and highly susceptible to cross-interference.[19,25] In addition, in order to avoid indiscriminate driving of enzymatic catalytic elements, these strategies typically depend on hybridization entropy-driven spontaneous structure assembly, which greatly slows down the reaction efficiency.[26,27] The underlying cause for these limitations is the absence of a suitable encoding mechanism between multiple signals, which prevents them from converging to form a tandem and unified signaling link. Therefore, how to break the inherent mode of existing multiple system construction and realize the unified multiple signals encoding effectively is the core issue for the realization of multiple RNA in situ analysis.

CRISPR/Cas system consists of CRISPR motif, Cas effector protein, and guide RNA, includes Cas9, Cas12, Cas13, etc., and has been widely applied in gene editing, biotherapeutics, and biosensing.[28,29] The classical CRISPR/Cas system possesses the properties of PAM structure-dependent specific sequence recognition, forward sequence cleavage, and collateral cleavage activity (Cas12, Cas13, etc.).[29–31] These properties confer the CRISPR/Cas system with natural signal recognition, encoding, and output capabilities, and thus CRISPR/Cas has been hailed by researchers as the next-generation molecular diagnostic technology. However, multiple detection technology based on CRISPR/Cas system suffers from the following obstacles: 1) disordered collateral cleavage activity: Cas12 or Cas13 proteases, etc., non-specifically cleave reporter probes upon activation, and fail to achieve independent multiple signal outputs within individual system;[30,32–34] 2) unitary signal coding ability: PAM structure-dependent highly specific sequence recognition necessitates multiple guide RNA for detecting multiple targets in the CRISPR/Cas system, significantly increasing system complexity.[32,35,36] Presently, researchers adopt droplets and other assistances for reaction system segmentation or Cas protein structure modification to initially realize the multiple detection with CRISPR/Cas system, but the application scenarios are greatly limited.[36–38] Therefore, it could be considered as an attractive attempt to more ingeniously utilize the sequence recognition and cleavage characteristics of CRISPR/Cas system to construct a fundamentally innovative mode of multiple coding detection.

In this study, we innovatively proposed to utilize the precise mismatch modulation and T-PAM structure transformation mechanism to construct an original key probe (KP) encoder and couple it with CRISPR/Cas9 signal exporter to develop a novel Cas9 code key system (**Scheme 1**). CRISPR/Cas9, compared to Cas12 or Cas13, retains a high dependency on PAM structure and precise sequence recognition capability without collateral cleavage activity, yet simultaneously faces signal output issue. Accordingly, in the design of KP encoder, on the one hand, we regulate the sequence hybridization entropy value by active mismatch base introduction, which realizes the non-collateral cleavage activity-dependent autonomous signal output of Cas9 protease. On the other hand, the spatial blocking effect of loop encoding identification region and frame structure modulates the formation of PAM structure, which in turn successively adjusts the activation of Cas9. Through the above mechanism, multiple targets can specifically binding dissociate with the corresponding loop recognition regions, triggering the deconstructive reorganization of KP encoders to form coding products. These different coding products feature the identical sgRNA targeting sequences, thus only a single sgRNA/Cas9 complex is required to

be involved, realizing multiple-to-one tandem signaling coding. Furthermore, the Cas9 code key system could be integrated with a T-strand displacement amplification (T-SDA) signal amplifier element to construct a highly efficient, specific and sensitive multiple RNA rapid in situ imaging system for precise typing detection of formalin fixed paraffin-embedded (FFPE) sample from clinical tumor patient. The establishment of Cas9 code key system breaks the inherent mode of parallel reaction in conventional multiple detection methods, and provides powerful technical support for multiple RNA in situ analysis, thus contributing to more accurate heterogeneous tumor typing and mechanism investigation.

2. Results

2.1. Signal Output Mechanism of Cas9 Code Key System Based on Mismatch Modulation

The principal difference of CRISPR/Cas9 system compared to Cas12a or Cas13a is that Cas9 protease does not possess efficient collateral cleavage activity after target activation, and cannot cleave the F-Q fluorescent beacons to generate signal.[39] Therefore, the primary problem of Cas9 code key system, which is dominated by CRISPR/Cas9 system, lies in the design of non-collateral cleavage activity-dependent signaling output system. As shown in **Figure 1**a, in the classical CRISPR/Cas9 system, sgRNA/Cas9 complex is guided by PAM motif to cleave targeted double-stranded (ds) sequence P (≈20 nt), which produces a stable dsDNA product of ≈17 nt. However, the dsDNA product exists with a high *T*m value and cannot be freely dissociated to release fluorescent signal. How to reduce the high *T*m value of dsDNA product while not compromising sgRNA/Cas9 cleavage would be expected to realize autonomous signal output. Therefore, we proposed to actively introduce mismatched bases and thus reduce binding entropy value. N mismatched bases are voluntarily doped in the non-recognition sequence of P probe in form of successive mismatch or interval mismatch. In the non-cleaved condition, P probe maintains a stable binding state. After being cleaved, due to the existence of mismatched bases, dsDNA product sequence dissociates autonomously with lower *T*m value than conventional reaction temperature (37 °C), which leads to the release of fluorescence signal (Figure 1b,c).

In order to investigate the hybridization state of P probes under different mismatch base incorporation modes, we first simulated and calculated the hybridization structure, Gibbs free energy (ΔG), and melting temperature (*T*m) of P probes before and after Cas9 cleavage by NUPACK algorithm and ZIPFOLD software (Figures S1 and S2, Supporting Information). As shown in Figure 1b,c and Table S3 (Supporting Information), P probe in interval mismatch mode was more sensitive to entropy change triggered by cleavage than in successive mismatch mode. Especially after incorporating 2 mismatched bases or more, *T*m value of cleaved dsDNA product in interval mismatch mode was lower than reaction temperature, and tended to be automatically dissociated. Fluorescence assay results also further verified the above conclusion (Figure 1b,c; Figures S3, and S4, Supporting Information). By comparing the signal differences before and after P probe cleavage in different mismatch modes, it could be clearly observed that a nearly 18-fold signal-to-noise (S/N) ratio might be obtained when interval mismatches were performed with 2 bases. In addition, the simulation results of NUPACK algorithm revealed that the difference in hybridization free energy caused by various mismatched base type (AT or CG) was negligibly minor compared to active mismatch introduction behavior. Therefore, by introducing mismatched bases to regulate hybridization entropy value, we successfully constructed a Cas9 signaling output system that is not dependent on collateral cleavage activity (Figure 1d). The fluorescent signal release yield after Cas9 cleavage was calculated by comparing with the equivalent concentration of fluorescent beacons, which could reach more than 90%, further indicating the high feasibility of this strategy, thus laying the foundation for the subsequent construction of Cas9 code key system.

2.2. Signal Activation Mechanism of Cas9 Code Key System Based on T-PAM Structure Transformation

As mentioned above, the crucial point for Cas9 code key system to realize multi-detection lies in the construction of a tandem and unified signaling link to implement orderly signal recognition encoding and conversion output. The mismatch-regulated P probe structure provides an autonomous signaling paradigm for Cas9. On this basis, the L sequence is inserted into P probe structure as a specific encoding identification region, forming the basic framework of key probe (KP) encoder, containing loop encoding identification region and sgRNA recognition region (**Figure 2**a). The KP encoder and Cas9 signal exporter compose the Cas9 code key system collectively, and its design points are as follows: 1) spatial blocking effect of loop sequence and T-framework structure is utilized to regulate the formation of PAM structure, which in turn modulates the target-responsive activation of Cas9; 2) the binding free of target and loop sequence is leveraged to trigger the structural transformation of KP encoder to form a unified format P probe product; 3) the loop encoding identification region is independent of the sgRNA recognition region, such that multiple recognition signals can correspond to consistent sgRNA targeting sequence. Therefore, in general, the signaling pathway of Cas9 code key system can be summarized as follows: the spatial structural transformation of T-frame and PAM (T-PAM) in KP encoder is triggered by target binding, resulting in cascade activation of Cas9 to generate output signals by cleavage.

First, in order to verify the structural assembly and signaling mechanism of KP encoder, PAGE electrophoresis and simulated target S were employed to analyze the state of KP encoder under different conditions. The KP encoder band formed by the assembly of L and P probe could be clearly observed in lane 7. With the addition of S strand in lane 8, KP encoder band was weakened, with the appearance of L and S strand binding product and separate P probe structure (Figure 2a). The PAGE results verified that the introduction of target could trigger spatial structural transformation of KP encoder to form a stable sgRNA recognition product. Furthermore, the regulation of PAM structure is crucial for Cas9 code key system to realize target response activation. Among them, the position of PAM in KP encoder structure serves as a principal effect factor to maximize the spatial blocking effect. Thus, fluorescence intensity was employed to preliminarily analyze the effect of PAM on Cas9 code key target

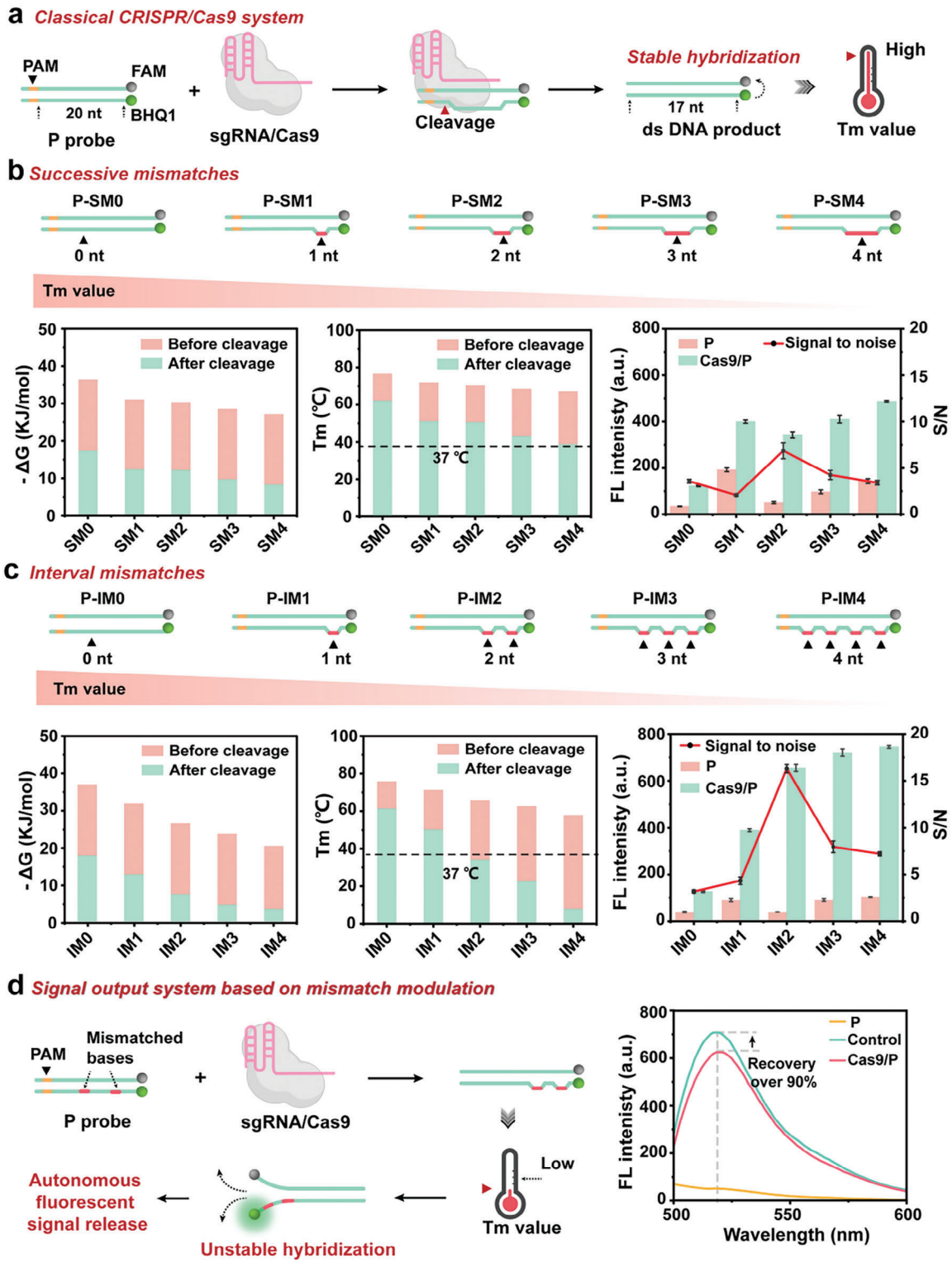

Figure 1. Mismatch modulation based Cas9 signaling output system. a) Schematic diagram of the classical CRISPR/Cas9 system. b) Simulated ΔG and *Tm* values of P probes introducing different numbers of mismatched bases in successive mismatch mode, and the fluorescence signal of these P probes after being cleaved by the CRISPR/Cas9 system. c) Simulated ΔG and *Tm* values of P probes introducing different numbers of mismatched bases in interval mode, and the fluorescence signal of these P probes after being cleaved by the CRISPR/Cas9 system. d) Schematic diagram of the Cas9 signaling output system based on entropy mismatch modulation and the fluorescence release of two-base interval mismatch P probe. Control group: fluorescent beacon at the same concentration as the P probe. Error bars indicate the standard deviation (mean ± SD, $n = 3$). The excitation wavelength was 490 nm and the emission wavelength was 518 nm.

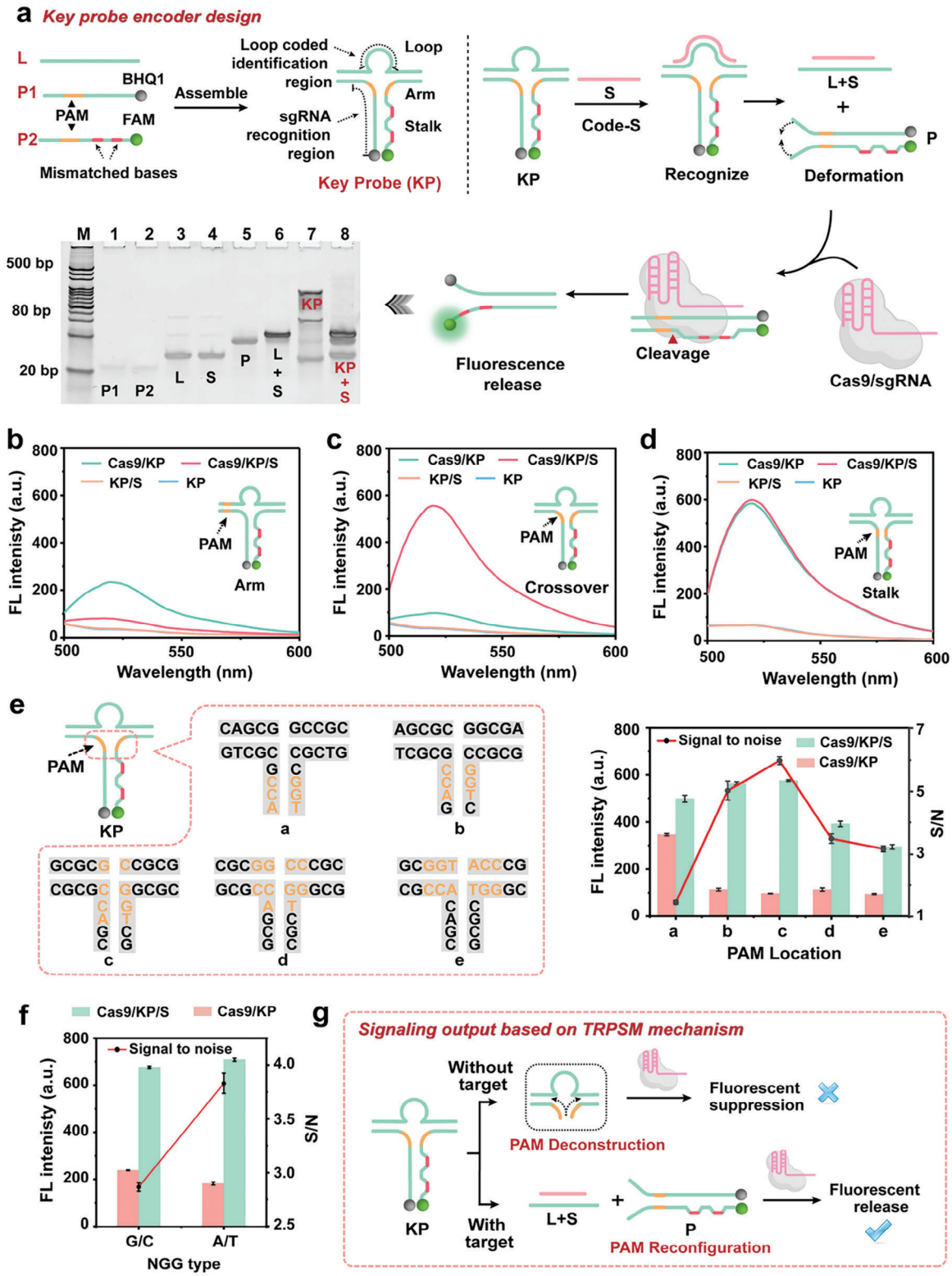

Figure 2. T-PAM structure transformation based Cas9 code key system. a) Schematic of the design of KP encoder and Cas9 code key system. In addition, KP encoder assembly was verified by PAGE electrophoresis. b–d) Fluorescence spectroscopy to verify the effect of PAM motifs located at different structural regions in KP encoder (arm, crossover, and stalk) on the CRISPR/Cas9 cleavage reaction. e) Schematic illustration of optimization of PAM located at crossover points and fluorescence validation results. f) Exploration of the base types of PAM sequences. g) Schematic of signal activation mechanism regulated by T-PAM structure transformation. Error bars indicate standard deviation (mean ± SD, $n = 3$). The excitation wavelength was 490 nm and the emission wavelength was 518 nm.

response activation when it was located in different structural regions (arm, crossover and stem) of KP encoder. The results indicated that when PAM sequence was in the arm and stem region of KP encoder, PAM could hybridize to form a complete structure, which could directly activate Cas9 protease system regardless of the presence or absence of target (Figure 2b,d; Figure S5, Supporting Information). In contrast, when the PAM structure was located in crossover region, it was difficult to hybridize completely due to the steric hindrance of loop identification region and the spatial site-blocking effect of frame assembly. Only when the introduction of S strand triggered the dissociation of L strand, the rehybridization of P probe could activate Cas9 protease recognition cleavage (Figure 2c). The above results strongly recommend that the spatial barrier could prevent the formation of PAM structure and thus regulate the activation of Cas9. Further, the particular location of PAM structure was more finely designed in the crossover region to obtain optimal signal-to-noise (S/N) ratio (Figure 2e). Finally, the commonly available *Streptococcus pyogenes*-derived (Spy) Cas9 protease native PAM sequence is 5′-NGG-3′, where N can be any of four deoxyribonucleotides.[39,40] The different hybridization bonding energy of A-T or C-G may impact on the formation of PAM structure. It was also confirmed by designing different PAM sequence comparisons that A-T base pairs with weaker hydrogen-bonding bond energy were more favorable to achieve spatial regulation of PAM (Figure 2f).

Overall, the structural transformation of T-PAM serves as a pivotal mechanism for target-responsive activation of Cas9 code key system (Figure 2g). Target-dependent binding triggers the deconstructive reorganization of T-frame, resulting in the complete assembly of PAM motifs, which in turn activates Cas9 protease successively. The successful establishment of this mechanism confirmed the initial feasibility of Cas9 code key system.

2.3. Exploration of Structure and Reaction Kinetics of Cas9 Code Key System

In order to obtain the optimal analysis performance of Cas9 code key system, we further explored influencing factors other than PAM structure. Considering the crucial role of spatial hindrance effect exerted by loop encoding identification region on the regulation of PAM structure, a series of loop sequences with different base numbers were designed for validation (**Figure 3a**). The results indicated that S/N ratio of Cas9 code key system increased gradually with the increase of loop base number (5–20 nt), but the further increase of base number beyond 20 nt resulted in a sharp decrease of S/N ratio, which might be attributed to the instability of KP encoder's entire structure due to excessively long loop sequence. In addition, the effect of mismatched base number in sgRNA recognition region on KP encoder was further explored. KP encoder structure is inherently more unstable compared to P probe due to higher free energy. Therefore, whether the appropriate number of mismatched bases for P probe is suitable for KP encoder structure still requires further validation. Figure 3b revealed that mismatching 2 bases apart remained to be the optimal choice. In order to increase the stability of KP encoder structure assembly, a series of parameters such as the concentration ratio of L/P1/P2, the annealing mode, and the concentration of Mg^{2+} utilized in annealing were systematically explored. Stable KP encoder assembly structure was obtained by applying the L/P1/P2 concentration ratio of 1.5:1:1 at 10 mM Mg^{2+} concentration and denaturing at 95 °C for 5 min followed by slow annealing at −1 °C min^{-1} (Figures S6–S8, Supporting Information).

On the basis of robust KP encoder structure, the optimal reaction conditions of Cas9 code key system were investigated. The code-S strand which simulates target signal drives the deconstructive reorganization of KP encoder through strand displacement reaction (SDR). The length of code-S strand inevitably affects the deconstructive efficiency of KP encoder. Therefore, a series of length gradients of code-S strand were set up to explore the optimal binding condition. The results revealed that the deconstruction of KP encoder was performed optimally when the length of coding S strand was 26 nt (Figure 3c). Longer code-S strand may result in decreased efficiency of strand displacement recognition due to their own secondary structure or dimerization behavior. In addition, the relative concentration ratio of KP encoder to sgRNA/Cas9 complex (1:2 optimal) and the reaction temperature (37 °C optimal) were further explored (Figures S9 and S10, Supporting Information).

Finally, we set up the classical target-mediated SDR as a comparison to investigate the reaction kinetics of Cas9 code key system. As shown in Figure 3d, the hybridization signal of hairpin probe H with simulated target S exhibited a slow rising trend with an initial rate of 1.0460 nM s^{-1}. On the contrary, Cas9 code key system reached signal peak within 20 min and the initial reaction rate reached 1.4148 nM s^{-1}, which was much higher than that of the classical SDR. The reason for this phenomenon could be attributed to the fact that the strand displacement hybridization between H and S involves a reversible reaction driven by entropy value. In contrast, KP encoder, after being deconstructed by S displacement, reorganizes to form a "product" P probe, which can activate Cas 9 protease, thus being continuously cleaved and consumed, resulting in an imbalance of potential energy between the two ends of SDR, which tends to accelerate the S-KP encoder displacement reaction in forward direction, and greatly improves the reaction efficiency. Furthermore, in contrast to the positively driven signal output system with irreversible Cas9 cleavage, the reversible strand displacement-driven reaction imposed constraints from thermodynamic equilibrium, leading to differences in the fluorescence signals of plateau phase between S-KP and S-H. These speculations were also confirmed by our previous study.[41]

2.4. Establishment and Performance Verification of Cas9 Code Key Multiple Detection System

The Cas9 code key multiple detection system relies on the loop encoding identification region of KP encoder and the T-PAM structural transformation of target response to realize the multiple target signal recognition encoding and conversion output. Therefore, we set up three KP encoders, and different KP encoders share the same sgRNA targeting sequence, while the main variation only lies in the sequence of loop recognition region and the fluorescent motif labeled at end of P probe. Through the specific hybridization binding of different coding strands with KP encoders, distinctive fluorescence signals can be generated for P probe cleavage corresponding to different

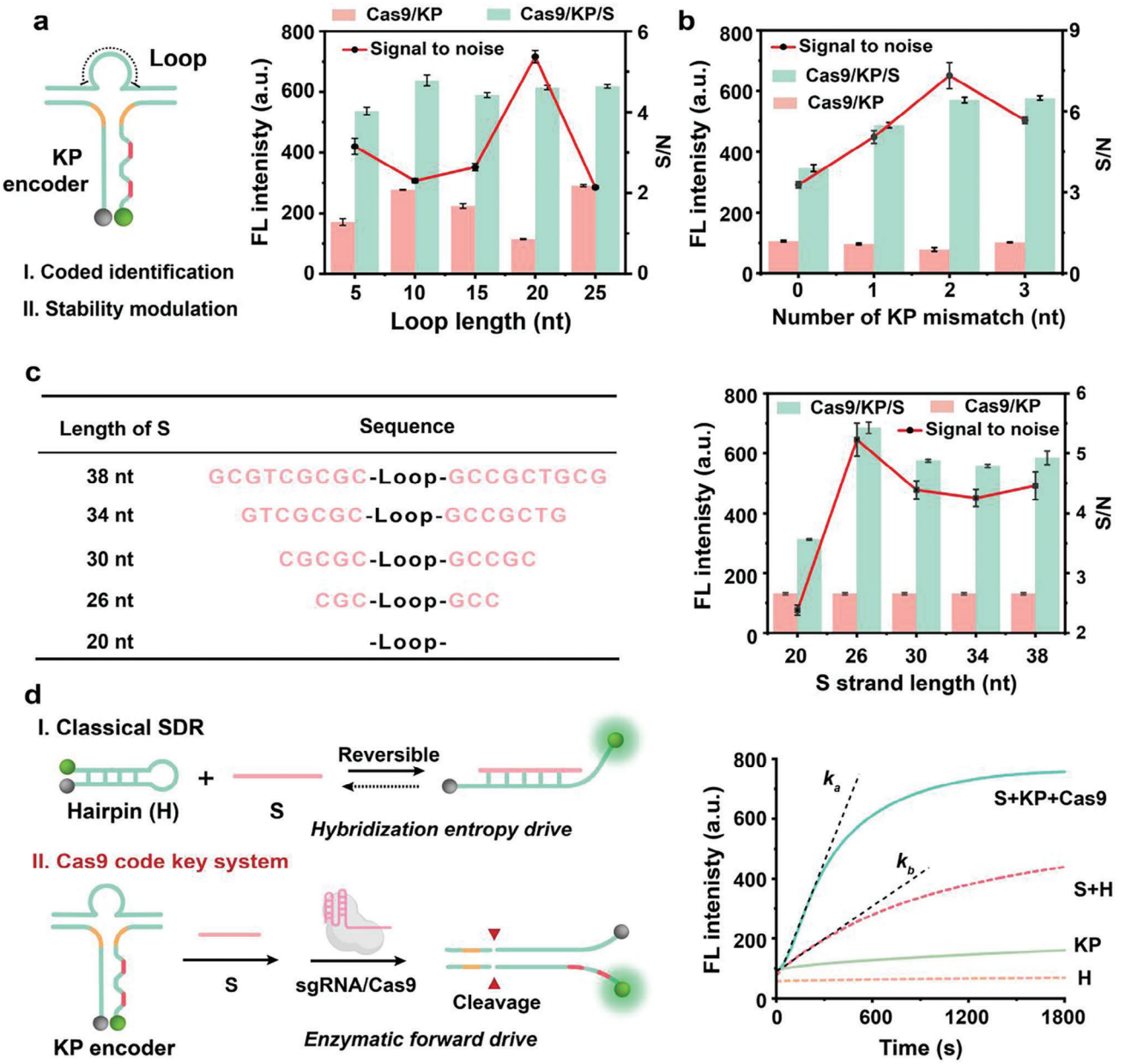

Figure 3. Exploration of structure and reaction kinetics of Cas9 code key system. a) Verification of the effect of loop length on the stability of KP encoder. b) Verification of the effect of the number of mismatched bases on KP encoder. c) Exploration of code-S strand length. d) Comparison of fluorescence reaction kinetics between classical SDR reaction and Cas9 code key system. Error bars indicate standard deviation (mean ± SD, $n = 3$). The excitation wavelength was 490 nm and the emission wavelength was 518 nm.

coding sequences in the presence of single sgRNA/Cas9 complex (**Figure** 4a). The results of Figure 4b fully verified the feasibility of Cas9 code key to realize multi-target detection within a single system, and three coding strands were eventually recovered to produce corresponding strong fluorescence signals. Notably, due to the highly specific binding of coding strand to corresponding loop identification region (20 nt complementary), the signals between multiple targets within single system were mutually non-interfering with each other, with almost no cross-reactivity, which fully demonstrated the specificity of this multiple detection strategy (Figure 4c). We further designed a series of mismatch targets (mismatches of 2, 4, and 6 bases and complete mismatches) to complement the selectivity experiments. The results indicated that KP encoder could effectively distinguish mismatched code sequences and maintain acceptable recognition specificity (Figure S11, Supporting Information).

In order to preliminarily explore the analytical performance of the Cas9 code key multiple detection system, coding strands with different concentration gradients were mixed within one single system under optimal reaction conditions and

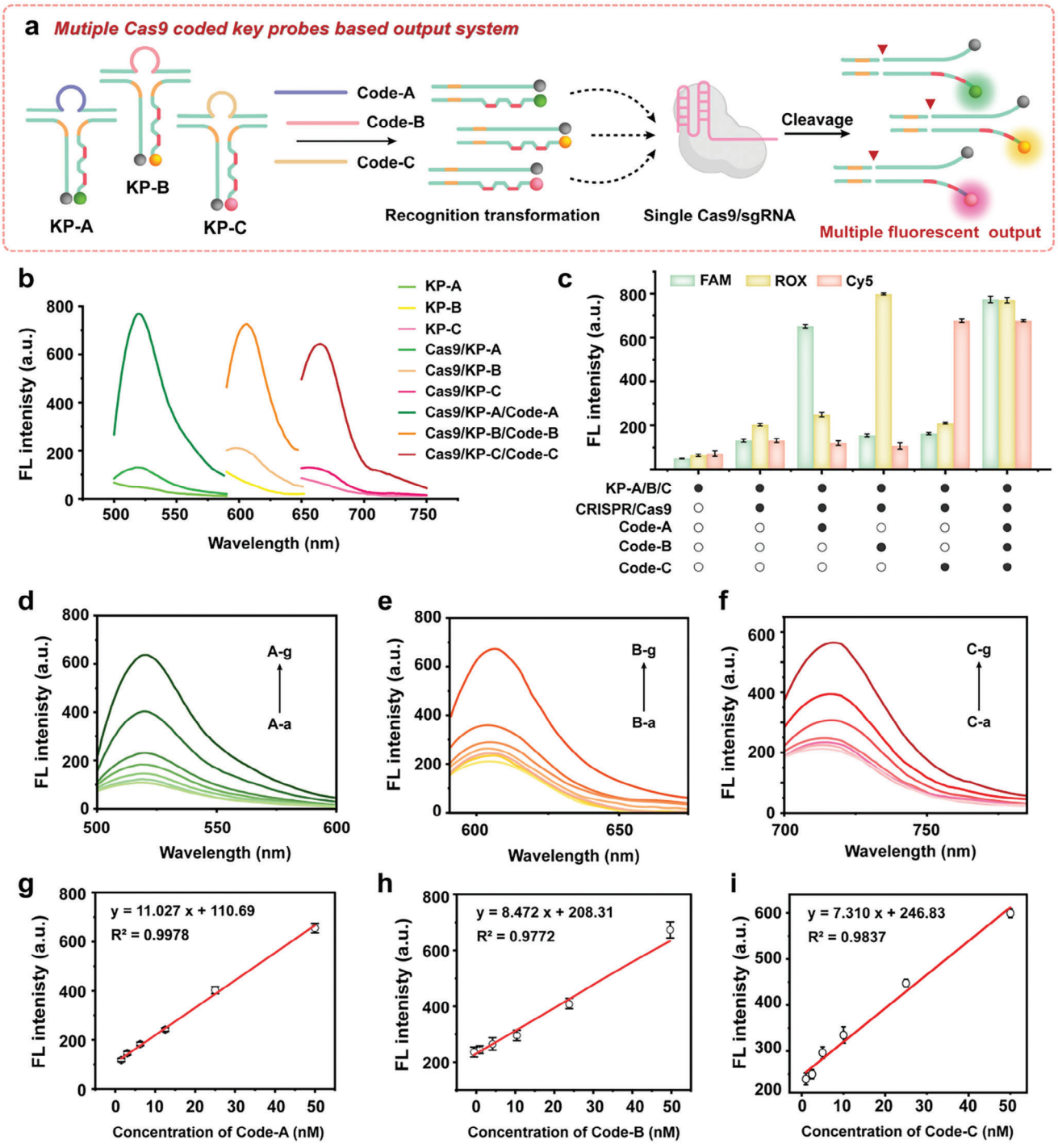

Figure 4. Validation of Cas9 code key multiple detection system. a) Schematic diagram of Cas9 code key multiple detection system. b) Feasibility validation of Cas9 code key multiple detection system. c) Target specificity exploration of Cas9 code key multiple detection system. d–f) Validation of the analytical performance of Cas9 code key multiple detection system. d–f) represented the fluorescence signal spectra triggered by a series of concentration gradients of Code-A, Code-B, and Code-C (0, 1, 2.5, 5, 10, 25, 50 nM, corresponding to A-a to A-g, B-a to B-g, and C-a to C-g, respectively). g–i) Linear calibration graphs (mean ± SD, $n = 3$) of fluorescence intensity at 518, 612, and 664 nm versus different coding strand concentrations. The excitation and emission wavelengths were set to 490 and 518 nm for the FAM channel, 580 and 612 nm for the ROX channel, and 630 and 664 nm for the Cy5 channel.

quantitatively analyzed. The results indicated that corresponding fluorescence signals of the single system gradually enhanced as the concentrations of Code-A, Code-B, and Code-C were progressively increased from 0 to 50 nM, respectively (Figure 4d–f), and exhibited a favorable linear relationship within the concentration gradient range (Figure 4g–i). Furthermore, according to the 3σ/slope rule, the limits of detection (LOD) were calculated to be 0.88, 0.93, and 0.61 nM, respectively. This result fully demonstrated that Cas9 code key multiple detection signal behaved reliably in concentration-dependent manner, which established the foundation for the subsequent construction of multiple mRNAs in situ imaging system.

2.5. Construction of Multiple RNA Rapid In Situ Imaging Strategy Based on Cas9 Code Key System

The superior analytical performance of Cas9 code key multiple detection system encouraged us to further develop in situ multiple RNA imaging strategy for rapid and precise typing of heterogeneous tumor. However, we clearly recognized that the absence of Cas9 protease collateral cleavage activity facilitated the construction of multiple detection system, but simultaneously lost the self-signal amplification ability, thus the sensitivity in analyzing extremely low abundance of tumor RNA targets was still insufficient. Therefore, inspired by the high-efficiency T-strand displacement amplification (T-SDA) signal amplifier element constructed in previous studies,[42,43] we introduced two primer TP strands to form a nicked T structure with target RNA, which triggered high-efficiency SDA signal amplification under the action of KF DNA polymerase and NB.BbvCI nick endonuclease to generate numerous repetitive signal strands, which then coupled to the subsequent Cas9 code key multiple detection system, and finally constructed a novel Cas9 code key-based multiple RNA rapid in situ imaging system (**Figure 5**a).

In this study, breast cancer cells were selected as the analytical model, and human epidermal growth factor receptor 2 (HER2), progesterone receptor (PR), and estrogen receptor (ER) mRNAs, which serve as molecular typing indicators for clinical breast cancer, were employed as targets for multiple assays. We initially validated the feasibility of Cas9 code key-based multiple RNA rapid in situ imaging system with SKBR3 (high expression of HER2, low expression of PR/ER mRNA). The lack of any component, such as SDA primer and KP encoder, failed to produce obvious fluorescence signal, and only when the complete Cas9 code key system was operated, clear in situ imaging results could be obtained, with S/N ratio up to 100-fold (Figure 5b; Figure S11, Supporting Information). Multiple mRNAs imaging of single SKBR3 cell indicated that HER2 mRNA expression remained at the highest level and mainly localized in the cytoplasm, while PR and ER mRNAs expression were reatively low, which was in line with the cellular characteristics (Figure S12, Supporting Information). The above results fully demonstrated that the proposed in situ imaging strategy possesses the ability to reliably analyze multiple mRNAs in situ. On this basis, we further explored the optimal reaction time of this system. By observing the in situ cellular imaging results in a series of time gradients, it was striking to observe that stable and clear fluorescence imaging results could be obtained at 60 min (Figure 5c). Compared with conventional in situ imaging techniques, the detection rate of Cas9 code key-based multiple RNA in situ imaging system was dramatically improved, which was mainly attributed to the fact that both signal amplification, multiple coding, and signal output were all driven by highly efficient enzymes rather than slow hybridization entropy. Moreover, it was worth mentioning that the Cas9 code key-based multiple RNA in situ imaging system required only one-step addition operation, avoiding extensive cumbersome processes, which was the main reason for realizing rapid imaging.

Furthermore, we choosed three cell models, MCF-10A (negative control), SKBR3 (high expression of HER 2, low expression of PR/ER mRNA), and MCF-7 (low expression of HER 2, high expression of PR/ER mRNA) to validate the in situ multiple imaging performance of Cas9 code key, and compared with qRT-PCR quantitative data of cell-extracted mRNA. Confocal laser scanning microscopy (CLSM) results revealed the presence of bright multiple fluorescent signals in all three cell models, which were fully consistent with mRNA expression profiles of each cell line (Figure 5d; Figure S14, Supporting Information). Additionally, comparison with qRT-PCR results indicated that multiple mRNA in situ imaging of three cell types analyzed by Cas9 code key were corresponded with qRT-PCR quantitative trend. All above results fully proved that Cas9 code key-based multiple RNA in situ imaging system possesses the ability of in situ multiple mRNAs imaging analysis, and exhibited the performance advantages of efficiency, sensitivity, and specificity, which could be expected to be further applied to actual clinical samples.

2.6. Clinical FFPE Sample Validation with Cas9 Code Key Based Multiple RNA Rapid In Situ Imaging System

To further explore the clinical potential of Cas9 code key based multiple RNA rapid in situ imaging system, we collected formalin-fixed and paraffin-embedded (FFPE) tissue slice samples from clinical breast cancer patients for HER2, PR, and ER mRNAs in situ imaging analysis. Classical immunohistochemistry (IHC) or fluorescence in situ hybridization (FISH) techniques are currently employed in clinical practice for the detection of breast cancer typing indices. However, both IHC or FISH are laborious to perform in situ detection of multiple markers in one FFPE sample, and cumbersome procedure (>24 h) greatly slows down clinical reporting time. In contrast, Cas9 code key based multiple RNA in situ imaging system enables rapid multiple mRNAs in situ imaging in less than 1 h by virtue of its efficient, sensitive and specific performance advantages (**Figure 6**a). We first utilized FFPE samples that were definitively diagnosed by clinical IHC/FISH for imaging validation of the proposed system. The results illustrated that Cas9 code key based multiple RNA in situ imaging system could effectively and simultaneously achieve clear imaging of three mRNAs in individual FFPE sample with high concordance by comparison with clinically graded diagnostic results (Figure 6b). Noticeably, the expression of PR/ER mRNA in the four samples was assessed at different clinical diagnostic hierarchies, and the imaging results similarly confirmed the abundance discrepancy. The above results demonstrated the practicality of Cas9 code key based multiple RNA in situ imaging system in FFPE sample analysis.

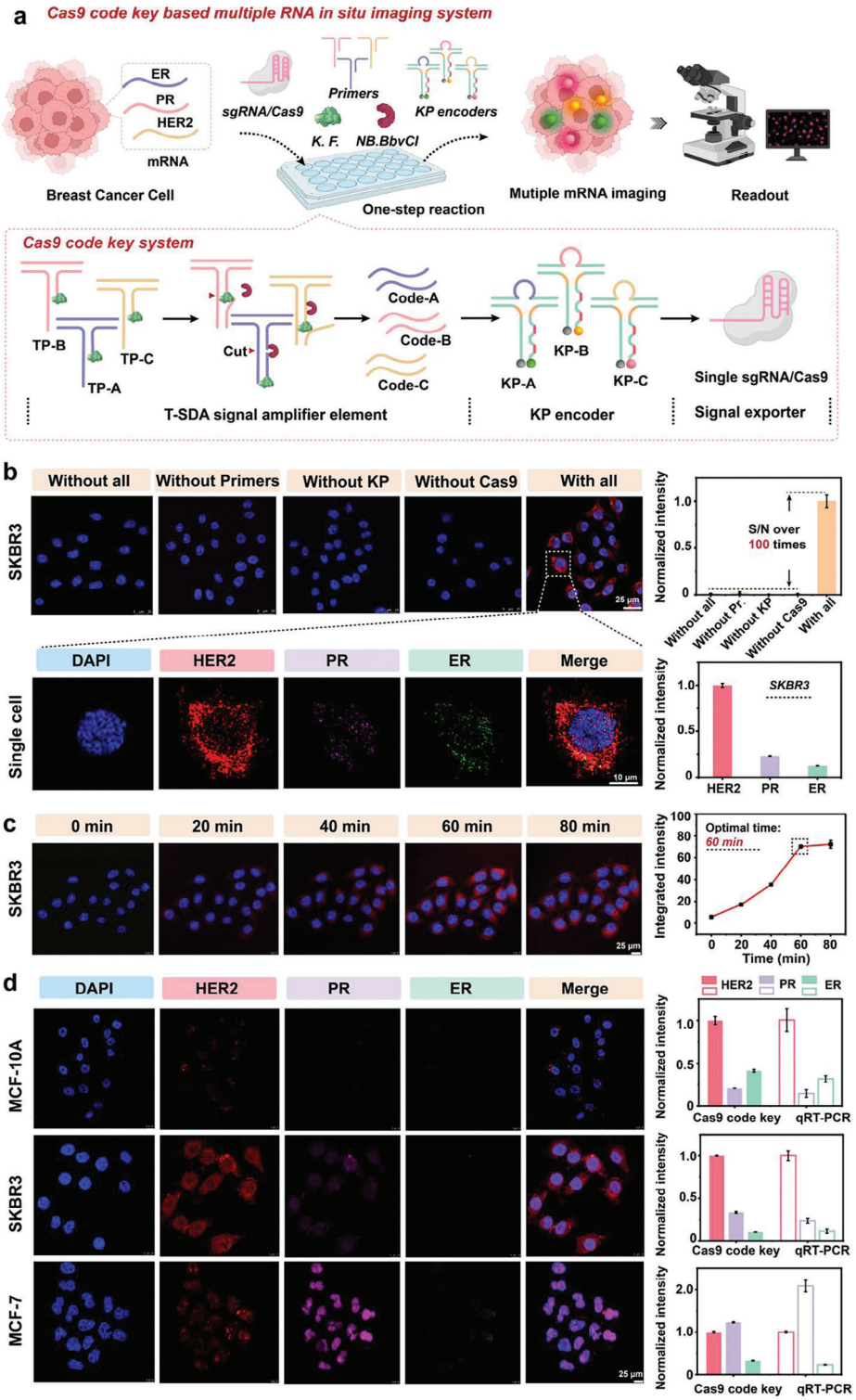

Figure 5. Cas9 code key based multiple RNA in situ imaging system. a) Schematic diagram of Cas9 code key based multiple mRNAs in situ imaging system. b) Feasibility validation of the proposed system, which was utilized to image SKBR3 (high HER2 expression, low PR/ER expression). Scale bar is 25 μm. Fluorescence imaging results of HER2, PR, and ER mRNAs in individual SKBR3 cell is highlighted in the figure. Scale bar is 10 μm. mRNA in situ imaging results were also quantified. c) Reaction time optimization of this in situ imaging system. Scale bar is 25 μm. d) Multiple mRNAs in situ imaging analysis of MCF-10A (negative control), SKBR3 (high HER2 expression, low PR/ER expression), and MCF-7 (low HER2 expression, high PR/ER expression) by the proposed system. Scale bar is 25 μm. Error bars indicate standard deviation (mean ± SD, $n = 3$). The excitation light channels employed were 405 nm (DAPI, blue), 488 nm (FAM, green), 561 nm (ROX, magenta), and 642 nm (Cy5, red), respectively.

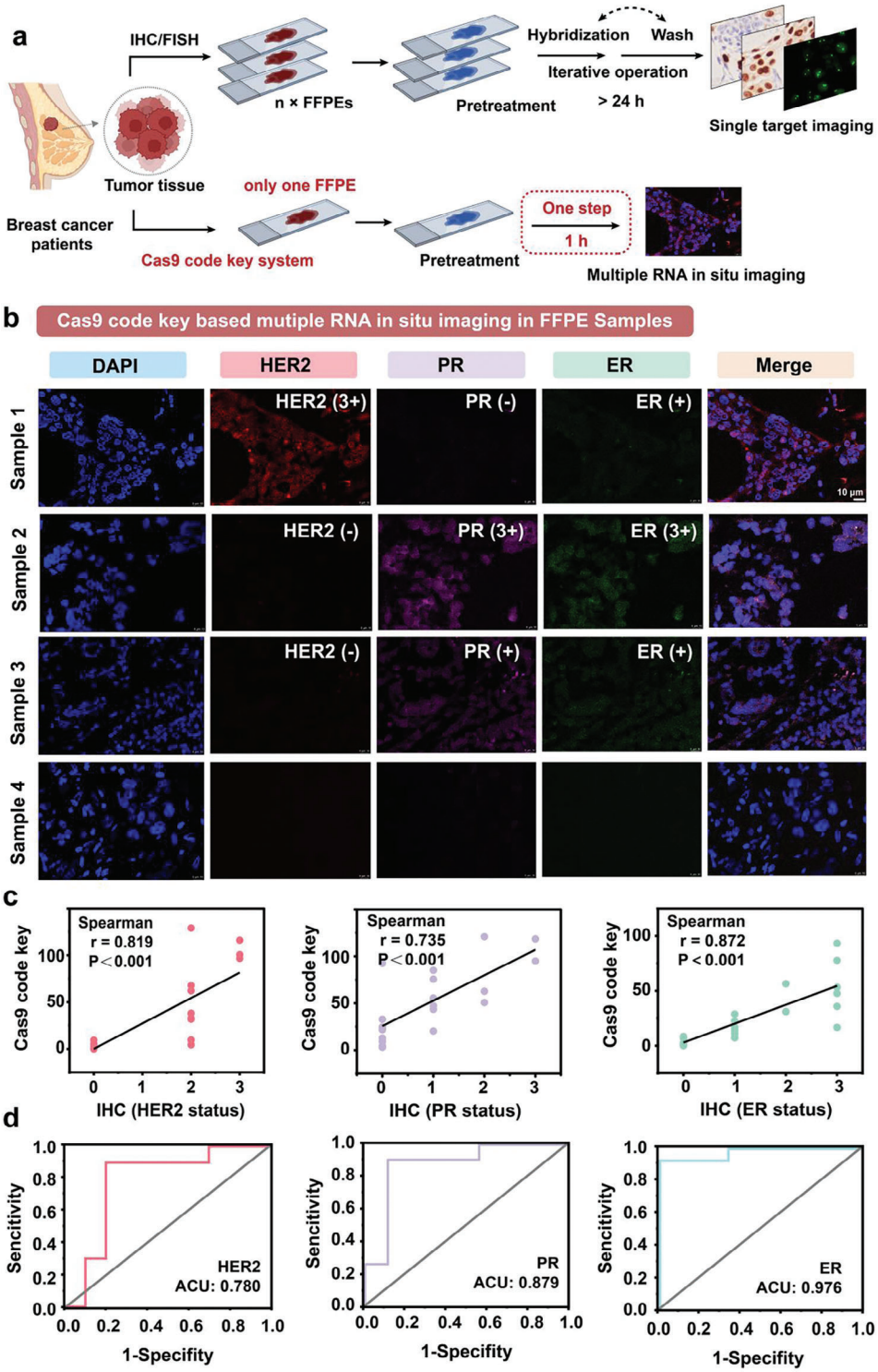

Figure 6. Cas9 code key system for multiple RNA in situ analysis in breast cancer FFPE samples. a) Illustration of the workflow of the Cas9 code key based multiple RNA rapid in situ imaging system versus existing clinical in situ molecular imaging systems. b) Multiple RNA imaging analysis of four clinical FFPE samples with different breast cancer subtypes by the proposed system. Scale bar is 10 μm. White labels in the imaging results are the clinical IHC grade of corresponding indicator. The excitation light channels employed were 405 nm (DAPI, blue), 488 nm (FAM, green), 561 nm (ROX, magenta), and 642 nm (Cy5, red), respectively. c) Spearman's correlation analysis of Cas9 code key system imaging results of HER2, PR, and ER typing indicators with clinical IHC/FISH grading results. d) ROC analysis of Cas9 code key multiple RNA imaging results compared with IHC/FISH grading results in the training cohort ($n = 20$). HER2 negativity was defined as IHC results of -, +, and 2+ (FISH negative), and HER2 positivity was defined as IHC results of 2+ (FISH positive) and 3+.PR and ER negativity was defined as IHC results of -. ER and PR positivity was defined as IHC results of +, 2+, and 3+.

On this basis, we further performed clinical comparative analysis of large samples. We collected 20 FFPE samples with different clinical breast cancer phenotypes, performed multiple mRNAs imaging by Cas9 code key, and compared with clinical IHC/FISH grading results (Figures S15–S17 and Table S14, Supporting Information). The Spearman correlation analysis demonstrated a significant correlation between the IHC/FISH grading and the quantitative fluorescence imaging results of Cas9 code key based multiple RNA in situ imaging system. More specifically, the Spearman correlations between the Cas9 code key-based mRNA imaging results of three indicators, HER2, PR, and ER, with the IHC/FISH grading were 0.819, 0.735, and 0.872, respectively, and $P < 0.001$ (Figure 6c). In addition, we performed ROC analysis of three metrics with IHC-positive cutoff values of +, 2+ and 3+ for ER and PR, and 2+ (FISH+) and 3+ for HER2. In the assessment of the area under the ROC curve (AUC), the AUCs for HER2, PR, and ER were 0.780, 0.879, and 0.976, respectively (Figure 6d), which fully demonstrated that the Cas9 code key based multiple RNA in situ imaging system offered high diagnostic accuracy. The above results confirmed that the multiple mRNAs in situ imaging analysis by Cas9 code key was highly consistent with clinical typing diagnosis, and exhibited broad clinical translational application prospect with the remarkable performance advantages compared with existing technologies.

3. Discussion

RNA, as the core link of central law, performs an essential role in genetic information transmission and protein function translation, and the abnormal expression of RNA has been confirmed by numerous studies to be closely related to tumor progression. Therefore, the precise analysis of RNA could be considered as an equally valuable approach for tumor molecular diagnosis. However, compared with DNA and protein, there is a lack of sophisticated clinical in situ analysis of RNA for tumor molecular typing. Strategies such as RNAscope, Stellaris RNA FISH, and π-FISH rainbow, which were constructed in previous studies, are limited by inefficiency of complex DNA self-assembly and high cost, which prevents them from being widely disseminated. In addition, tumor heterogeneity determines the necessity of multiple RNA analysis, whereas multiple assays in above strategies are mainly based on the inherent pattern of parallel repetitive reaction, which greatly increases system complexity. Therefore, efficient, rapid, and specific multiple RNA in situ analysis strategy is urgently demanded by clinical necessary technical support, which is also the main foothold of this study.

As mentioned in the introduction, the crucial factors for multi-target analysis are specific target identification, multi-link signal encoding, and non-interfering signal outputs, which require a tandem and uniform signal transmission mechanism among multiple signals. Therefore, in this study, we originally proposed a cas9 code key system, which efficiently realizes multi-signal detection through mismatch modulation and T-PAM structure transformation mechanism. In this system, the KP encoder skillfully utilizes the spatial barrier effect of loop encoding identification region to regulate the formation of PAM structure. It realizes the activation of target-responsive Cas9 signal exporter through the binding free of target and loop while generating encoding product P probe. The introduction of mismatched bases in P probe greatly enhances the variation difference in *T*m value before and after Cas9 cleavage, thus realizing the autonomous output of fluorescent signal at routine reaction temperature. Remarkably, the loop encoding identification region in KP encoder wanders outside the sgRNA recognition region. This configuration enables the sgRNA recognition regions between various KP encoders to maintain the identical sequence. Consequently, only a single sgRNA/Cas9 complex is required to realize multiple signal outputs, enabling multiple-to-one tandem signal encoding.

Furthermore, we coupled the T-SDA signal amplifier element at the fore end of KP encoder, and then constructed a rapid multiple RNA in situ imaging strategy based on Cas9 code key system. Benefiting from efficient amplification of T-SDA and multiplexing performance of Cas9 code key system, the strategy realized multiple RNA in situ imaging in FFPE samples from clinical breast cancer patients. Surprisingly, the results revealed that the proposed strategy could obtain clear multiple RNA imaging profile within 1 h with only one sampling operation, which exhibited a tremendous performance advantage over existing clinical in situ analysis strategies, such as FISH, IHC, and so on. Moreover, this strategy was utilized to evaluate 20 FFPE samples from breast cancer patients with different typing diagnoses. The multiple RNA in situ imaging results obtained were in high concordance with clinical diagnostic grading, which fully confirmed the reliable potential of this strategy for clinical application. However, it remains to be mentioned that the limitation of this strategy is the relatively restricted fluorescence encoding capacity, resulting in the inability to expand more detection pathways.

Overall, the Cas9 code key system proposed in this study abandons the conventional mode of parallel in situ analysis strategy based on nucleic acid self-assembly and provides a fresh tandem coding paradigm for multiple detection system construction. The multiple RNA rapid in situ imaging strategy based on Cas9 code key system demonstrated astonishing analytical performance, which is promising to provide a revolutionary technical support for clinical tumor molecular typing and mechanism exploration.

4. Experimental Section

Materials: DNA oligonucleotides were purchased from Sangon Biotechnology Co. Ltd. (Shanghai, China). RNA oligonucleotide was purchased from Tsingke Biotechnology Co. Ltd. (Beijing, China). *S.pyogenes* Cas9 Nuclease, 10× NEBuffer r3.1 [1 M NaCl, 500 mM Tris-HCl, 100 mM $MgCl_2$, 1 mg mL^{-1} recombinant albumin, pH 7.9], klenow fragment (3′→5′ exo), NB.BbvCI, and dNTP were purchased from New England Biolabs (Ipswich, MA, USA). Diethyl pyrocarbonate (DEPC)-treated water, Tris-EDTA (TE) buffer [10 mM Tris-HCl, 0.1 mM EDTA, pH 8.0], 5× TBE buffer [445 mM Tris, 445 mM boric acid, 10 mM EDTA, pH 8.0-8.6], 20× saline-sodium citrate (SSC) buffer (DEPC treated) [3 M NaCl, 300 mM sodium citrate, pH 6.9-7.1], 20× phosphate buffered saline (PBS) (DEPC treated) [200 mM Na_2HPO_4, 35 mM KH_2PO_4, 2.74 M NaCl, 53 mM KCl, pH 7.2-7.6], GelRed, PAGE gel fast preparation kit, xylene, and ethanol were obtained from Sangon Biotechnology Co. Ltd. (Shanghai, China). 6× Loading buffer and 20-base pair DNA marker were obtained from Takara Biotech. Inc. (Dalian, China). Dulbecco's modified eagle's medium (DMEM), RPMI 1640 medium, and FBS were obtained from Thermo Fisher Scientific Inc. (USA). PBS [8 mM Na_2HPO_4, 136 mM NaCl, 2 mM KH_2PO_4, 2.6 mM KCl, pH 7.0-7.2], paraformaldehyde universal tissue fixative (4%), and Triton X was obtained from Biosharp Life Science (Beijing, China). 4′,6-Diamidino-2-phenylindole (DAPI) was purchased from

Beyotime Institute of Biotechnology (Shanghai, China). SPARKeasy Cell RNA Kit, SPARKscriptII RT Plus Kit (with gDNA eraser), and 2× SYBR Green qPCR Mix (with ROX) were purchased from Sparkjade Co., Ltd. (Shandong, China). Tris-magnesium (TM) buffer [20 mM Tris-HCl, 50 mM $MgCl_2$, pH 7.9] was self-prepared. All buffer solutions were prepared and diluted using DEPC-treated water.

DNA/RNA Oligomers: The sequences of all DNA oligonucleotides were synthesized according to the specifications in Tables S2, S4–S12 (Supporting Information), while the sequences of RNA strands were synthesized based on Table S1 (Supporting Information). DNA strands were first dissolved in TE buffer and stored at 20 µM at −20 °C. RNA oligonucleotide was dissolved in DEPC-treated water and similarly stored at a concentration of 20 µM at −20 °C for future use.

Preparation of P Probe and KP Encoder: P probe and KP encoder were prepared through DNA self-assembly. P1 and P2 with different numbers of mismatched bases were incubated in TM buffer at 37 °C for 30 min in an equimolar ratio to form 500 nM P probe. To fabricate 500 nM KP encoder, P1, P2, and L were mixed in a 1:1:1.5 ratio in TM buffer. The annealing process began at 95 °C for 5 min, followed by a gradual cooling down to 25 °C at a rate of −1 °C min^{-1}. P probe and KP encoder were stored at 4 °C for future use.

Mismatch Modulation Based Cas9 Code Key Signal Output System: To form the sgRNA/Cas9 complex, 50 nM spyCas9 and 75 nM sgRNA were pre-incubated in 1× NEBuffer r3.1 (diluted to 1× using DEPC-treated water before use) for 10 min at 37 °C in the MINIC-100 mini dry bath (HANU, China). The reaction system consisted of 50 nM sgRNA/Cas9, 25 nM P probe, and 1× NEBuffer r3.1 in a 100 µL reaction volume. The reaction was carried out at 37 °C for 20 min. For mismatch modulation based Cas9 code key signal output system, the reaction system consisted of 50 nM pre-incubated sgRNA/Cas9, 25 nM KP-A, 25 nM Code-A strand, and 1× NEBuffer r3.1 in 100 µL reaction volume. The reaction was performed at 37 °C for 20 min.

Classical SDR Reaction Based on Hairpin: The hairpin was formed by slowly annealing process that began at 95 °C for 5 min, followed by a gradual cooling down to 25 °C at a rate of −1 °C min^{-1}. The reaction system consisted of 25 nM hairpin, 25 nM Code-A, and 1× NEBuffer r3.1 in 100 µL reaction volume.

Cas9 Code Key Based Multiple Detection System: spyCas9 (150 nM) with 225 nM sgRNA were first incubated in 1× NEBuffer r3.1 for 10 min at 37 °C to constitute sgRNA/Cas9 complex before cleavage assay. The reaction system consisted of 150 nM pre-incubated sgRNA/Cas9, 25 nM each of KP-A, KP-B, and KP-C, various concentrations of each of Code-A, Code-B, and Code-C strands, and 1× NEBuffer r3.1 in 100 µL reaction volume. The reactions were performed at 37 °C for 20 min.

Fluorescence Measurement: Fluorescence intensity was measured by Cary Eclipse (Agilent Technology, USA). The fluorescence intensity of three channels (FAM, ROX, and Cy5) was measured with a volume of 100 µL. The excitation and emission wavelengths were set to 490 and 518 nm for the FAM channel, 580 and 612 nm for the ROX channel, and 630 and 664 nm for the Cy5 channel. The silt widths of excitation and emission were both 1.5 nm.

Fluorescence Reaction Kinetics: Fluorescence reaction kinetics were measured via F-4700 fluorometer (Hitachi, Japan). Cas9 code key system consisted of 50 nM pre-incubated sgRNA/Cas9, 25 nM KP-A, and 1× NEBuffer r3.1. The hairpin reaction system included 25 nM hairpin probe (H) and 1× NEBuffer r3.1. Both measurements began after the addition of 25 nM Code-A into the reaction system. The reaction temperature was maintained at 37 °C. Fluorescence intensity was recorded at 1 s intervals for 1800 s, with an excitation wavelength of 490 nm and an emission wavelength of 518 nm. The silt widths of excitation and emission were both 1.5 nm.

Polyacrylamide Gel Electrophoresis (PAGE) Analysis: Polyacrylamide gel electrophoresis was conducted using a 12% gel prepared with a PAGE gel fast preparation kit, operated at 110 V in a 1× TBE buffer. Subsequently, 10 µL of sample solution and 2 µL of 6× loading buffer were mixed and added to each loading well. After the separation in the electrophoresis apparatus (Bio-Rad Laboratories, Singapore), the gels containing DNA were stained using GelRed and visualized by Bio-Rad ChemDoc XRS Imaging System (Bio-Rad Laboratories, USA).

Cell Culture: The human breast cancer cell lines MCF-7 and SKBR3 were cultured in DMEM medium supplemented with 10% fetal bovine serum (FBS), penicillin (100 U mL^{-1}), and streptomycin (100 µg mL^{-1}) at 37 °C in a humidified atmosphere containing 5% CO_2. The human breast cancer cell line MCF-10A was cultured in DMEM/F12 medium supplemented with 20 ng mL^{-1} EGF, Hdrycortisone Insulin, NEAA, 5% HS, 1% P/S solution at 37 °C in a humidified atmosphere containing 5% CO_2.

Multiple RNA Rapid In Situ Imaging Strategy Based on Cas9 Code Key System: Cells were grown to a density of 40% to 50% on 14-mm cell slides in 24-well plates. The cells were then fixed using 4% paraformaldehyde universal tissue fixative and subsequently rinsed with PBS. Following fixation, the cells were permeabilized with 5% Triton X. Cas9 code key system consisted of 1 µM each of KP-A, KP-B, and KP-C, 500 nM each of T-HER2, T-ER, and T-PR, 500 nM each of P-HER2, P-ER, and P-PR, 6 µM pre-incubated sgRNA/Cas9, 10 mM dNTP, 10 U Klenow fragment (3′→5′ exo), 3 U NB.BbvCI, and 1× NEBuffer r3.1. The reaction system was incubated on prepared MCF-7, MCF-10A, and SKBR3 fixed cells for 1 h at 37 °C. After staining with DAPI for 5 min, the cells were immediately observed via Leica TCS SP8 STED confocal laser scanning microscopic (CLSM) (Leica, Germany). The excitation optical channels used were 405, 488, 561, and 642 nm, respectively.

Cellular Total RNA Extraction: Cellular total RNA was isolated from MCF-7, MCF-10A, and SKBR3 cells using SPARKeasy Cell RNA Kit following the manufacturer's protocol. The concentration of total RNA was determined by BioDrop µlite+ (BioDrop, USA).

Quantitative Reverse Transcription-Polymerase Chain Reaction (qRT-PCR): For the qRT-PCR analysis of HER2, ER, PR mRNAs, cDNA samples were synthesized by reverse-transcription from 0.5 µg total cellular RNA using SPARKscriptII RT Plus Kit (with gDNA eraser) according to the manufacturer's instructions (GAPDH as the reference gene). PCR was performed with 2× SYBR Green qPCR Mix (with ROX) on CFX96 Touch Real-Time PCR Detection System (Bio-Rad Laboratories, USA). The 10 µL of solution contained 2 µL of cDNA sample, 0.5 µL of forward primer (5 µM), 0.5 µL of reverse primer (5 µM), 5 µL of 2× SYBR qPCR Mix, and 2 µL of RNase free water. The PCR was performed in the following conditions: 95 °C for 3 min, 40 cycles of 95 °C for 15 s, and 60 °C for 30 s.

Multiple mRNAs In Situ Imaging of FFPE Samples: De-identified human breast cancer FFPE tissue sections and clinical data were obtained from the Department of Pathology of the First Affiliated Hospital of Chongqing Medical University. This study was approved by the Ethics Committee of the First Affiliated Hospital of Chongqing Medical University (2022-K461). FFPE tissue sections were baked at 60 °C for 1 h, and then the sections were dewaxed in fresh xylene and rehydrated in ethanol. Targets were retrieved for 20 to 30 min in 2× SSC buffer (DEPC treated) at 97 °C. Next, sections were washed in PBS (DEPC treated), and after thoroughly air-drying, they underwent treatment with pepsin working solution at 37 °C in the hybridizer (ThermoBrite, USA) for 18 min. Then rinsed with 2× SSC buffer (DEPC treated) at room temperature for 5 min, dehydrated with ethanol series (75%, 85%, and 100%), and allowed to air-dry. Sections were permeabilized with 5% Triton X at 37 °C for 5 min, followed by a single wash with 1× PBS (DEPC treated). After complete air-drying, the Cas9 code key based multiple RNA rapid in situ imaging system was applied using the method described above, and the CLSM imaging procedure was carried out.

Statistical Analysis: All data were processed using Origin 2021. The reproducibility of the results was evaluated through a minimum of three independent experiments. In the legend, "*n*" signified the number of independent experiments conducted.

Supporting Information

Supporting Information is available from the Wiley Online Library or from the author.

Acknowledgements

R.H., W.Y., and J.L. contributed equally to this work. The authors acknowledge financial support from the projects of National Natural Science Foundation of China (82372334, 81873972, 82202634, 82272432); Chongqing Science Fund for Distinguished Young Scholars (cstc2019jcyjjqX0028); Foundation for Innovative Research Groups of Chongqing Higher Education Institutions (CXQT20013); Chongqing Talents-Innovation Leading Talents Project (CQYC20210302385, cstc2022ycjhbgzxm0001); The First Affiliated Hospital of Chongqing Medical University Top Talent Training Program (BJRC2022-02); Zhejiang Provincial Health Bureau (2023RC126, 2023ZF001); Chongqing Natural Science Foundation (cstc2020jcyj-msxmX0237); Hainan Provincial Health Industry Research Project Fund (22A200151).

Conflict of Interest

The authors declare no conflict of interest.

Data Availability Statement

The data that support the findings of this study are available from the corresponding author upon reasonable request.

Keywords

CRISPR/Cas9, FFPE sample, key probe encoder, multiple RNA in situ imaging, tumor typing

Received: February 7, 2024
Revised: March 29, 2024
Published online:

[1] M. C. Haffner, W. Zwart, M. P. Roudier, L. D. True, W. G. Nelson, J. I. Epstein, A. M. De Marzo, P. S. Nelson, S. Yegnasubramanian, *Nat. Rev. Urol.* **2021**, *18*, 79.
[2] A. Gavish, M. Tyler, A. C. Greenwald, R. Hoefflin, D. Simkin, R. Tschernichovsky, N. Galili Darnell, E. Somech, C. Barbolin, T. Antman, D. Kovarsky, T. Barrett, L. N. Gonzalez Castro, D. Halder, R. Chanoch-Myers, J. Laffy, M. Mints, A. Wider, R. Tal, A. Spitzer, T. Hara, M. Raitses-Gurevich, C. Stossel, T. Golan, A. Tirosh, M. L. Suvà, S. V. Puram, I. Tirosh, *Nature* **2023**, *618*, 598.
[3] S. Bärthel, C. Falcomatà, R. Rad, F. J. Theis, D. Saur, *Nat. Cancer* **2023**, *4*, 454.
[4] J. Peng, B.-F. Sun, C.-Y. Chen, J.-Y. Zhou, Y.-S. Chen, H. Chen, L. Liu, D. Huang, J. Jiang, G.-S. Cui, Y. Yang, W. Wang, D. Guo, M. Dai, J. Guo, T. Zhang, Q. Liao, Y. Liu, Y.-L. Zhao, D.-L. Han, Y. Zhao, Y.-G. Yang, W. Wu, *Cell Res.* **2019**, *29*, 725.
[5] D. A. Lawson, K. Kessenbrock, R. T. Davis, N. Pervolarakis, Z. Werb, *Nat. Cell Biol.* **2018**, *20*, 1349.
[6] Q. Zeng, M. Mousa, A. S. Nadukkandy, L. Franssens, H. Alnaqbi, F. Y. Alshamsi, H. A. Safar, P. Carmeliet, *Nat. Rev. Cancer* **2023**, *23*, 544.
[7] R. Vegliante, I. Pastushenko, C. Blanpain, *EMBO J.* **2022**, *41*, 109221.
[8] F. Wu, J. Fan, Y. He, A. Xiong, J. Yu, Y. Li, Y. Zhang, W. Zhao, F. Zhou, W. Li, J. Zhang, X. Zhang, M. Qiao, G. Gao, S. Chen, X. Chen, X. Li, L. Hou, C. Wu, C. Su, S. Ren, M. Odenthal, R. Buettner, N. Fang, C. Zhou, *Nat. Commun.* **2021**, *12*, 2540.
[9] J. Qian, S. Olbrecht, B. Boeckx, H. Vos, D. Laoui, E. Etlioglu, E. Wauters, V. Pomella, S. Verbandt, P. Busschaert, A. Bassez, A. Franken, M. V. Bempt, J. Xiong, B. Weynand, Y. Van Herck, A. Antoranz, F. M. Bosisio, B. Thienpont, G. Floris, I. Vergote, A. Smeets, S. Tejpar, D. Lambrechts, *Cell Res.* **2020**, *30*, 745.
[10] T.-Q. Zhang, Z.-G. Xu, G.-D. Shang, J.-W. Wang, *Mol. Plant* **2019**, *12*, 648.
[11] C. Buccitelli, M. Selbach, *Nat. Rev. Genet.* **2020**, *21*, 630.
[12] H. J. Johansson, F. Socciarelli, N. M. Vacanti, M. H. Haugen, Y. Zhu, I. Siavelis, A. Fernandez-Woodbridge, M. R. Aure, B. Sennblad, M. Vesterlund, R. M. Branca, L. M. Orre, M. Huss, E. Fredlund, E. Beraki, Ø. Garred, J. Boekel, T. Sauer, W. Zhao, S. Nord, E. K. Höglander, D. C. Jans, H. Brismar, T. H. Haukaas, T. F. Bathen, E. Schlichting, B. Naume, J. Geisler, S. Hofvind, O. Engebråten, et al., *Nat. Commun.* **2019**, *10*, 1600.
[13] L. Zhang, Y. Zhang, C. Wang, Y. Yang, Y. Ni, Z. Wang, T. Song, M. Yao, Z. Liu, N. Chao, Y. Yang, J. Shao, Z. Li, R. Zhou, L. Chen, D. Zhang, Y. Zhao, W. Liu, Y. Li, P. He, J. Lin, Y. Wang, K. Zhang, L. Chen, W. Li, *Signal Transduction Targeted Ther.* **2022**, *7*, 9.
[14] J. E. Bradner, D. Hnisz, R. A. Young, *Cell* **2017**, *168*, 629.
[15] R. T. Davis, K. Blake, D. Ma, M. B. I. Gabra, G. A. Hernandez, A. T. Phung, Y. Yang, D. Maurer, A. E. Y. T. Lefebvre, H. Alshetaiwi, Z. Xiao, J. Liu, J. W. Locasale, M. A. Digman, E. Mjolsness, M. Kong, Z. Werb, D. A. Lawson, *Nat. Cell Biol.* **2020**, *22*, 310.
[16] H. Chen, J. Yao, R. Bao, Y. Dong, T. Zhang, Y. Du, G. Wang, D. Ni, Z. Xun, X. Niu, Y. Ye, H.-B. Li, *Mol. Cancer* **2021**, *20*, 29.
[17] M. Kreuz, D. J. Otto, S. Fuessel, C. Blumert, C. Bertram, S. Bartsch, D. Loeffler, S.-H. Puppel, M. Rade, T. Buschmann, S. Christ, K. Erdmann, M. Friedrich, M. Froehner, M. H. Muders, S. Schreiber, M. Specht, M. I. Toma, F. Benigni, M. Freschi, G. Gandaglia, A. Briganti, G. B. Baretton, M. Loeffler, J. Hackermüller, K. Reiche, M. Wirth, F. Horn, *Eur. Urol.* **2020**, *78*, 452.
[18] S. Das, M. Vera, V. Gandin, R. H. Singer, E. Tutucci, *Nat. Rev. Mol. Cell Biol.* **2021**, *22*, 483.
[19] C.-H. L. Eng, M. Lawson, Q. Zhu, R. Dries, N. Koulena, Y. Takei, J. Yun, C. Cronin, C. Karp, G.-C. Yuan, L. Cai, *Nature* **2019**, *568*, 235.
[20] M. Hong, S. Tao, L. Zhang, L.-T. Diao, X. Huang, S. Huang, S.-J. Xie, Z.-D. Xiao, H. Zhang, *J. Hematol. Oncol.* **2020**, *13*, 166.
[21] F. Wang, J. Flanagan, N. Su, L.-C. Wang, S. Bui, A. Nielson, X. Wu, H.-T. Vo, X.-J. Ma, Y. Luo, *J. Mol. Diagn.* **2012**, *14*, 22.
[22] D. Schulz, V. R. T. Zanotelli, J. R. Fischer, D. Schapiro, S. Engler, X.-K. Lun, H. W. Jackson, B. Bodenmiller, *Cell Syst.* **2018**, *6*, 25.
[23] P. Zhu, Y. Wang, J. Wu, G. Huang, B. Liu, B. Ye, Y. Du, G. Gao, Y. Tian, L. He, Z. Fan, *Nat. Commun.* **2016**, *7*, 13608.
[24] Y. Tao, X. Zhou, L. Sun, D. Lin, H. Cai, X. Chen, W. Zhou, B. Yang, Z. Hu, J. Yu, J. Zhang, X. Yang, F. Yang, B. Shen, W. Qi, Z. Fu, J. Dai, G. Cao, *Nat. Commun.* **2023**, *14*, 443.
[25] K. H. Chen, A. N. Boettiger, J. R. Moffitt, S. Wang, X. Zhuang, *Science* **2015**, *348*, aaa6090.
[26] S. He, R. Bhatt, C. Brown, E. A. Brown, D. L. Buhr, K. Chantranuvatana, P. Danaher, D. Dunaway, R. G. Garrison, G. Geiss, M. T. Gregory, M. L. Hoang, R. Khafizov, E. E. Killingbeck, D. Kim, T. K. Kim, Y. Kim, A. Klock, M. Korukonda, A. Kutchma, Z. R. Lewis, Y. Liang, J. S. Nelson, G. T. Ong, E. P. Perillo, J. C. Phan, T. Phan-Everson, E. Piazza, T. Rane, Z. Reitz, et al., *Nat. Biotechnol.* **2022**, *40*, 1794.
[27] C. R. Merritt, G. T. Ong, S. E. Church, K. Barker, P. Danaher, G. Geiss, M. Hoang, J. Jung, Y. Liang, J. McKay-Fleisch, K. Nguyen, Z. Norgaard, K. Sorg, I. Sprague, C. Warren, S. Warren, P. J. Webster, Z. Zhou, D. R. Zollinger, D. L. Dunaway, G. B. Mills, J. M. Beechem, *Nat. Biotechnol.* **2020**, *38*, 586.
[28] J. Y. Wang, J. A. Doudna, *Science* **2023**, *379*, add8643.
[29] A. Pickar-Oliver, C. A. Gersbach, *Nat. Rev. Mol. Cell Biol.* **2019**, *20*, 490.
[30] S.-Y. Li, Q.-X. Cheng, J.-K. Liu, X.-Q. Nie, G.-P. Zhao, J. Wang, *Cell Res.* **2018**, *28*, 491.
[31] J. S. Chen, E. Ma, L. B. Harrington, M. Da Costa, X. Tian, J. M. Palefsky, J. A. Doudna, *Science* **2018**, *360*, 436.

[32] R. Bruch, G. A. Urban, C. Dincer, *Trends Biotechnol.* **2019**, *37*, 791.
[33] J. S. Gootenberg, O. O. Abudayyeh, M. J. Kellner, J. Joung, J. J. Collins, F. Zhang, *Science* **2018**, *360*, 439.
[34] J. S. Gootenberg, O. O. Abudayyeh, J. W. Lee, P. Essletzbichler, A. J. Dy, J. Joung, V. Verdine, N. Donghia, N. M. Daringer, C. A. Freije, C. Myhrvold, R. P. Bhattacharyya, J. Livny, A. Regev, E. V. Koonin, D. T. Hung, P. C. Sabeti, J. J. Collins, F. Zhang, *Science* **2017**, *356*, 438.
[35] Y. Li, L. Liu, G. Liu, *Trends Biotechnol.* **2019**, *37*, 792.
[36] M. Karlikow, E. Amalfitano, X. Yang, J. Doucet, A. Chapman, P. S. Mousavi, P. Homme, P. Sutyrina, W. Chan, S. Lemak, A. F. Yakunin, A. G. Dolezal, S. Kelley, L. J. Foster, B. A. Harpur, K. Pardee, *Nat. Commun.* **2023**, *14*, 1505.
[37] Y. Zhao, D. Chen, Z. Xu, T. Li, J. Zhu, R. Hu, G. Xu, Y. Li, Y. Yang, M. Liu, *Anal. Chem.* **2023**, *95*, 3476.
[38] Y. Shang, G. Xing, J. Lin, Y. Li, Y. Lin, S. Chen, J.-M. Lin, *Biosens. Bioelectron.* **2024**, *243*, 115771.
[39] F. Jiang, J. A. Doudna, *Annu. Rev. Biophys.* **2017**, *46*, 505.
[40] D. Ma, Z. Xu, Z. Zhang, X. Chen, X. Zeng, Y. Zhang, T. Deng, M. Ren, Z. Sun, R. Jiang, Z. Xie, *Nat. Commun.* **2019**, *10*, 560.
[41] X. Cheng, X. Li, Y. Kang, D. Zhang, Q. Yu, J. Chen, X. Li, L. Du, T. Yang, Y. Gong, M. Yi, S. Zhang, S. Zhu, S. Ding, W. Cheng, *Nucleic Acids Res.* **2023**, *51*, gkad953.
[42] J. Xu, M. Liu, W. Zhao, S. Wang, M. Gui, H. Li, R. Yu, *J. Hazard. Mater.* **2022**, *429*, 128347.
[43] Y. Zhao, L. Zhou, Z. Tang, *Nat. Commun.* **2013**, *4*, 1493.